High-resolution diapycnal mixing map of the Alboran Sea thermocline from seismic reflection images

Jhon F. Mojica[1-2], Valentí Sallares[2], Berta Biescas[2-3]

[1] Center for Global Sea Level Change – NYUAD, Abu Dhabi UAE.
[2] Institute of Marine Sciences-CSIC, Barcelona, Spain
[3] Consiglio Nazionale delle Ricerche-ISMAR, Bologna, Italy

Correspondence to: Jhon F. Mojica (jfm11@nyu.edu)

Abstract. The Alboran Sea is a dynamically active region where the salty and warm Mediterranean water first encounters the incoming milder and cooler Atlantic water. The interaction between these two water masses originates a set of sub-mesoscale structures and a complex sequence of processes that entail mixing close to the thermocline. Here we present a high-resolution map of the diapycnal diffusivity around the thermocline depth obtained using acoustic data recorded with a high-resolution multichannel seismic system. The map reveals a patchy thermocline, with areas of strong diapycnal mixing juxtaposed with others of weaker mixing. The patch size is of a few km in the horizontal scale and of 10-15 m in the vertical one. The comparison of the obtained maps with the original acoustic images shows that mixing tends to concentrate in areas where internal wave become unstable and shear instabilities develop. These results are also compared with others obtained using conventional probes. The values estimated based on the seismic data are within the ranges of values obtained from oceanographic data analysis, and they are also consistent with reference theoretical values. Overall, our results demonstrate that high-resolution seismic systems allow to remotely quantify mixing at the thermocline depth with a lateral resolution of O(10^1 m).

KEYWORDS: Thermocline mixing, Seismic Oceanography, Diapycnal diffusivity map.

1. INTRODUCTION

Diapycnal diffusivity (k_ρ) around the thermocline plays a major role to control the strength and pattern of the ocean circulation, because it determines heat and salt heterogeneity at different spatial scales. This process usually occurs in a vertically stratified regime, affecting adjacent layers with the same density but different temperature and salinity (Stewart, 2008). In terms of processes, mixing in the ocean can be separated in two categories. One is related to internal wave (IW) breaking, which produces turbulent motion and changes the density stratification; while the second concerns the development of high frequency dynamic instabilities that are formed due to shear (Gregg, 1987; D'Asaro and Lien, 2000). As the spatial scale decreases, mixing leads to an unbalanced pressure field that eventually results in a collapse and dispersion of mixing waters through isopycnals (Thorpe, 2005). The value of k_ρ depends on the buoyancy frequency (N) and the dissipation rate (ε) as indicated by the so-called Osborn (1980) relationship:

$$k_\rho = \Gamma \varepsilon / N^2 \quad (1)$$

This value, where $\Gamma = 0.2$ is the empirically defined mixing efficiency (Osborn and Cox, 1972), corresponds to the mixing between isopycnal layers in the thermocline. The global mean k_ρ value

is of the order of $10^{-4}\ m^2s^{-1}$ (Munk and Wunsch, 1998), which corresponds to the value required to keep overturning in the thermocline. It has been shown that if $k_\rho < 10^{-5}\ m^2s^{-1}$ there is not enough energy to generate mixing (Gregg, 1989).

In a conservative flow, ε might present small variation due dissipated heat through turbulent motions, but in the presence of strong shear, ε tends to increase (Thorpe, 2005), reaching a maximum value close to the Kolmogorov scale (Gargett and Holloway, 1984). Good knowledge of its behavior provides important clues on available energy and its transfer between spatial scales.

The loss rate of kinetic energy in the turbulent motion is commonly expressed as:

$$\varepsilon = \left(\frac{\nu}{2}\right)\langle S_{ij}S_{ij}\rangle \quad (2)$$

$$S_{ij} = \left(\frac{\partial u_i}{\partial x_j} + \frac{\partial u_j}{\partial x_i}\right) \quad (3)$$

Where $\nu = 1.064x10^{-6}\ m^2s^{-1}$ is the kinematic viscosity and the tensor S_{ij} is a function of the velocity components in the three orthogonal directions (Thorpe, 2005). Conventional in-situ techniques as Vertical Microstructure turbulence Profiler (VMP) or microriders provide the most accurate measures of k_ρ, but in just one dimension. In general, although measures are accurate in the vertical dimension, sampling in the horizontal direction is much poorer, particularly in the $\sim 10^3$-$10^1\ m$ range (Klymak and Moum, 2007 a, b). Since this is the range of scales at which the transition between isotropic internal wave and anisotropic turbulence motion (i.e. mixing) occurs, the observational evidence of mixing patterns and the understanding of the underlying physical mechanisms are rather limited so far. Overall, direct measures and observations are too few to create a global mixing map with the required resolution to feed the models with appropriate dissipation ranges (Smyth et al., 2011). This makes it in turn difficult to integrate mixing into large-scale ocean dynamics models. Its effects are simulated instead through the incorporation of eddy diffusivity coefficients, which are tuned *ad hoc* to match the large-scale distribution of ocean observables. While this approach allows to properly reproduce regional spatial-temporal patterns, it severely hampers the long-term predictive capability of ocean dynamics and, in turn, that of climate models. Improving our knowledge on the short-term and small-scale mixing mechanisms and integrating them into large-scale models remain thus as an outstanding challenge.

To overcome this issue, remote sensing techniques have recently started to be used (e.g. Gibson et al., 2007). One of these alternative techniques is multichannel seismics (MCS), an acoustic method providing quasi-synoptic images of the thermohaline boundaries in the ocean interior to full ocean depth, with a lateral resolution of up to $\sim 10^1\ m$ (Holbrook et al., 2003). Several recent works have demonstrated that it is actually possible to map k_ρ using measures of the horizontal wavenumber (k_x) spectra of the vertical displacements of thermohaline boundaries imaged with MCS acquisition systems (Sheen et al., 2009; Holbrook et al., 2013; Fortin et al., 2016). However, these studies use conventional, relatively low-resolution systems with source energy concentrating below *~50 Hz*. In addition, these systems are not well suited to image the shallowest ocean layers (i.e. $< 200\ m$), but deeper water levels ($\geq 400\ m$ depth). At these depth levels, the changes in the internal structure

are usually less marked than those at shallower levels, and especially around the thermocline. In a recent work, it has been shown that high resolution MCS (HR-MCS) systems, which use a small energy, but higher-frequency source, allow imaging the thermohaline structure as shallow as *~30 m* with a lateral resolution of *12-15 m* and *1-~2 m* in the vertical direction (Sallares et al., 2016). This resolution is three- to four-fold better than that of conventional MCS systems used to image deeper ocean levels. Therefore, it has the potential to image sub-mesoscale structures and processes that affect the thermocline at scales of kilometers to tens of meters, allowing to cover the existing observational gap. Despite its potential, HR-MCS systems have never been used to date to quantify diapycnal mixing at the thermocline depth.

Here we use the above-mentioned method of extracting $k_\rho(x, z)$ maps from MCS images, but applied for the first time to HR-MCS data acquired in the Alboran Sea (Westernmost Mediterranean). The method to calculate diapycnal mixing maps from the horizontal wavenumber spectra of vertical reflector displacements is analogous to that proposed by Sheen et al. (2009) and Holbrook et al. (2013). The result is a high-resolution mixing map of the ocean at the thermocline depth (*30-110 m*) along a *35 km*-long transect (Fig. 1a). This method can be used in other regions where the water column is sufficiently stratified to record the acoustic impedance variations (density x sound speed contrasts between neighboring water layers).

The rest of the manuscript is structured as follows: in section 2 we present the hydrographic context, and the observations; then we describe the acquisition system and the method applied to estimate k_ρ from the seismic data. The results are described in section 3, whereas the discussion about the imaged structures and their likely causes is presented in section 4. Finally section 5 summarizes the main conclusions.

2. DATA AND METHODOLOGY

The Alboran Sea is characterized by the continuous exchange between Mediterranean Water (MW) and Atlantic Water (AW) through the Strait of Gibraltar. This exchange concentrates near the surface (between *~30 m* and *200 m*); where the shallow, moderately saline and cold incoming AW (*< 50 m*) interacts with the deeper, warmer, saltier and more stable outgoing MW, producing another water mass known as Modified Atlantic Water (MAW). In this framework, internal waves, strong horizontal shear instability, and prominent thermohaline stratification are generated. These particular features reflect the complex dynamic setting of the area, with kinetic energy being transferred between isopycnals from large to small scales, leading eventually to overturning, isotropic turbulence and irreversible mixing.

The data set used in this work, which includes collocated seismic and oceanographic measurements, was collected in the framework of the IMPULS-2006 experiment. Here, we concentrate our analysis on one of the seismic profiles (IMPULS-3), which was acquired on board the Spanish R/V Hesperides using a HR-MCS system. The acquisition started on May 16th at 23:43 and finished on May 17th at 04:00. In total, some 4 hours to record a 38 km-long profile. The acquisition system consisted of a 4.75 liters source with a peak frequency at 150-190 Hz. The corresponding size of the Fresnel zone, a proxy of the horizontal resolution (e.g. Sheriff and Geldart, 1995), is *12-15 m*. The streamer was 300 m-long and had 48 channels, with a group

spacing of 6.25 m. The shot interval was 15 m, giving a Common Mid-Point (CMP) gathers fold of 6. The location of the different data is displayed in Fig. 1a.

This profile was first processed and used to estimate the k_x energy spectra of the vertical displacements of the seismic reflectors. A total of 68 reflectors were tracked and used for the analysis (Sallares et al., 2016). As it is shown in this paper, the 68 reflectors are rather homogeneously distributed throughout the analyzed area. They have lengths of *1.5-21 km*, and a signal-to-noise ratio higher than *8* within the frequency range of *40–240 Hz*. Vertical profiles of temperature and pressure were recorded simultaneously with the seismic acquisition using 4 XBT's; whereas the salinity and buoyancy profiles were obtained from an XCTD, dropped three days after the seismic acquisition. Water current profiles have also been used in the study, but they are not coincident with the seismic acquisition (see location in Fig. 1a). They were obtained during the SAGAS experiment on board the Spanish R/V Sarmiento de Gamboa using an ADCP ocean surveyor 75, in the same season as the seismic experiment but 4 years later.

The HR-MCS profile shown in Fig. 2 reveals a number of laterally coherent seismic reflectors that are assumed to follow isopycnals (Biescas et al., 2014). The analysis of the obtained k_x spectra allowed identifying three sub-ranges that control dynamics around the thermocline depth at increasingly small spatial scales (Sallares et al., 2016). Thus at scales larger than the horizontal buoyancy wavelength ($l_N \approx 90\ m$), motions are dominated by the internal wave field (internal wave-field subrange). Then the spectra rolls off reflecting the presence of shear instabilities of probably the Kelvin-Helmholtz (KH) type, which appear to collapse at a scale of *~30 m* (transitional or instability-dominated subrange), giving rise to turbulence at even smaller scales (turbulent subrange). A more detailed description of these ranges and their scales is presented in Sallares et al. (2016). In the present work, we use the energy levels obtained from the k_x spectral analysis of the reflectors to estimate the variations of ε and k_ρ along the whole profile.

Since our dataset does not include direct measurements of turbulence, we use the XCTD and ADCP data to estimate a vertical profile of k_ρ based on Gregg's (1989) model; hereafter referred to as Gregg89. The Gregg89 model assumes that energy dissipation in the thermocline is made through IW energy transfer by wave-wave interaction. This model links shear current at different depths. The simplest way to obtain average dissipation rates over large space and time scales is through:

$$\varepsilon = 7x10^{-10}\, N^2/N_0^2 < S_{10}^4/S_{GM}^4 > \quad (4)$$

$$S_{10}^4 = 4.22[(\Delta U/\Delta z)^2 + (\Delta V/\Delta z)^2]^2 \quad (5)$$

$$S_{GM}^4 = 2[(3\pi/2) j_x E_{GM} b N_0^2 k^c (N/N_0)^2]^2 \quad (6)$$

Where $N_0 = 5.2\ x10^{-3}\ s^{-1}$ is the reference buoyancy frequency, S_{10} is the shear variance calculated from the meridional (*V)* and zonal (*U*) velocity variations according to the depth (*Z*), S_{GM} is the

variance for the Garret-Munk model (Gregg, 1989), j_x is a mode number, E_{GM} is the Garrett-Munk energy density, b is a scale factor, and k is the horizontal wavenumber.

Alternatively, the model proposed by Batchelor (1959); hereafter referred as Batchelor59, estimates k_ρ as a function of the energy transfer from large to small scales in the turbulent regime. This model assumes that the energy exchange from mechanical to caloric due to N and ε can be approximated as:

$$\varphi_\zeta^T = \left(\frac{4\pi\Gamma}{N^2}\right) C_T \varepsilon_T{}^{2/3} (2\pi k)^{-5/3} \quad (7)$$

Where φ_ζ is the energy spectrum of the isopycnals vertical displacement; and C_T is a proportionality constant (Sreenivasan, 1996). We apply this model to estimate the mixing rates over the seismic profiles applying a method proposed and described in previous works, (i.e. Sheen et al., 2009; Holbrook et al., 2013). The main steps of this approach are described below.
To identify the dissipation signature in the seismic profile, we first calculate the energy level in the turbulent subrange from our data by averaging the value obtained for all reflectors within 1200 m-wide and 15 m-high windows. Longer tracks are cut to fit inside the window. As it is explained in Sallares et al. (2016), this does not affect the spectrum at the spatial scale range analyzed. We then apply Batchelor59 model, Eq. (7), to estimate ε using the obtained energy level within the window (transitional subrange), with $\Gamma=0.2$, $C_T=0.3$ and N is calculated according to depth. Finally, we apply Eq. (1) using the $\varepsilon(x, z)$ values obtained above to estimate $k_\rho(x, z)$. These steps are repeated within windows of the size mentioned above that slide *30 m* in the horizontal direction and *3 m* in the vertical at eachnew analyzing step. The fact that we incorporate few new data at each step, produces a smoothly varying map instead of the one with sharp bounds that would be obtained without overlapping windows (e.g. Sheen et al., 2009; Holbrook et al., 2013).

In summary, both Gregg89 and Batchelor59 models are used to estimate mixing rates from two independent data sets: XCTD-ADCP and seismic data, respectively. The results obtained using both models are then compared to gain confidence in the proposed methodology. We then analyze and discuss the high-resolution 2D map resulting from the seismic data in terms of mixing.

3. RESULTS

A smoothly varying k_ρ map that covers the whole profile (Fig. 3) were obtained applying the sliding window approach explained above. The goal is being able to identify features and processes occurring in the transition between the internal wave and the turbulence sub-regimes, such as the intensity and scales of variability of the mixing patches, the location and size of the hotspots and their potential relationship with oceanographic features such as IWs or shear instabilities.

3.1. Probe-based $k_\rho(z)$ profile

To have a reference value to compare with the MCS-based $k_\rho(x,z)$ maps, we have first calculated a $k_\rho(z)$ profile for shallow waters (< *200 m*) using the XCTD and ADCP data and applying the

Gregg89 model (Eqs. 4-6). To do this we have used ADCP measures averaged within 10 m-depth bins. By doing this, we obtain an average value for the shear variance of $S_{10}^4 = 0.28\ s^{-1}$, whereas the reference value of the shear variance obtained from the Garrett-Munk model (Gregg, 1989) is $S_{GM}^4 = 0.013\ s^{-1}$. This gives an average dissipation rate $\langle\varepsilon\rangle \approx 1.3x10^{-8}\ Wkg^{-1}$, and an average diapycnal diffusivity $\langle k_\rho \rangle \approx 10^{-3.0}\ m^2s^{-1}$ for the targeted depth range (Fig. 4a). The $k_\rho(z)$ profile obtained from the XCTD and ADCP is also shown in Fig. 4a, together with the global averages for overturning ($\langle k_\rho \rangle \approx 10^{-4}\ m^2s^{-1}$) as well as the average pelagic diffusivity in the ocean ($\langle k_\rho \rangle \approx 10^{-5}\ m^2s^{-1}$).

We obtain minimum values of the mixing rate at *50-55 m*, *68-73 m*, and *100-125 m*. The absolute minimum of $k_\rho = 10^{-5.2}\ m^2s^{-1}$ is obtained at *~115 m*, whereas the maximum is of $10^{-2.1}\ m^2s^{-1}$ at *~15 m*. This gives a range of variation of $10^{-3.1}\ m^2s^{-1}$. Deeper than this, the mixing variability is smaller. The Turner angle and buoyancy frequency (Fig. 4b) indicate that the region is mostly stable with a slight tendency to double-diffusion ($Tu \sim 45^\circ$).

It is worth noting that, at this specific location, the average vertical $\varepsilon(z)$ and $k_\rho(z)$ values are one order of magnitude higher that the global average ones. The higher values probably reflect the effect of overturning in the thermocline. While probe-based measurements are well suited to investigate mixing variability in the vertical dimension, they do not provide information on the variability in the horizontal dimension with a comparable level of detail. As explained above, to do this we have used estimations of ε and k_ρ based on the HR-MCS data, but applying Batchelor59 model (Eq. 7) in this case.

3.2. High-resolution multichannel seismics-based $k_\rho(x, z)$ map

The $k_\rho(x, z)$ map displayed in Fig. 3 has average values of $\langle\varepsilon\rangle \approx 6.5x10^{-9}\ Wkg^{-1}$ and $\langle k_\rho \rangle \approx 10^{-2.7}\ m^2s^{-1}$. These values are within the range of values obtained from the XCTD and ADCP data but, at the same time, they are over an order of magnitude higher than the global ocean reference value of $k_\rho \approx 10^{-4.0}\ m^2s^{-1}$ (Fig. 4a). Figure 5 displays the $k_\rho(x, z)$ map superimposed with the HR-MCS data. It is interesting to note that the range of horizontal variability is similar to that observed in the vertical dimension, although there is no direct visual correspondence between the k_ρ anomalies and IWs. The range of variability is of over three orders of magnitude, locally reaching an extreme value of $k_\rho \approx 10^{-1.5}\ m^2s^{-1}$ at a depth of *~55 m* and at *16 km* along the line; and a minimum value of $k_\rho \approx 10^{-4.5}\ m^2s^{-1}$ at *~95 m* depth and *20 km* along the line, which is close to the global oceanic average. Numerous patches with k_ρ values exceeding $10^{-2}\ m^2s^{-1}$ with a characteristic size of *1-2 kms* in the horizontal dimension and *~10 m.* in the vertical are found throughout the whole section (i.e., yellowish patches in Figs. 3 and 5). Not only the average depth value, but also the vertical size of the anomalies, as well as the range of k_ρ variation, are in agreement with the probe-based values (Fig. 4). The contribution of the high k_ρ patches to the local average is outstanding, raising it from a background average value of $\sim 10^{-4}\ m^2s^{-1}$ to $\sim 10^{-2.5}\ m^2s^{-1}$.

To try to understand the existing relationships between mixing variability and water dynamics, we analyze various reflectors to identify a possible visual correspondence between individual sub-mesoscale features and mixing hotspots. Among the numerous horizons examined, we show in fig. 5, three horizons named H1, H2, H3, which spatially coincide with anomalously, high and low

mixing patches. For these three horizons, we have analyzed the structures observed in the different sub-regimes.

3.3 Analysis of individual reflectors

H1 is located at ~*50 m* depth and has a length of ~*5.5 km* (*31.5-37 km* along profile). It was selected because it is laterally coherent for several kms and, it coincides with one of the high mixing hotspots (Fig. 5). Its corresponding k_x spectrum is displayed in Fig. 6a.

To calculate k_ρ over the whole horizon (Fig. 7a) we used the spectral energy obtained within a *1.2 km*-wide window moving laterally *30 m* at each step along the whole profile. To analyze the features that contribute to the energy spectrum in the different scales, and to compare them in turn with the k_ρ values obtained along the entire reflector length, the horizon has been filtered at wavelength bands attributed to the IW subrange (*3000-100 m*), and the instability dominated subrange (*100-30 m*, transitional subrange). As a reference, the local horizontal buoyancy wavelength, estimated from the XCTD data is $l_N \approx 90$ *m* (Sallares et al., 2016). The different spectral subranges that are observed in the combined spectrum of the 68 reflectors (fig. S1) is also observed in most individual spectra such as those displayed in fig. 6. One of the main features is the systematic steep slope spectra at the instability-dominated subrange, which is likely associated with the loss of energy in the wave field due to dissipation (e.g. Samodurov et al., 1995). As it is explained in Sallares et al. (2016), the variation of the slope spectra at the intermediate scale is consistent with numerical estimates for the evolutionary stage of the vortex sheet linked to shear instabilities (Waite, 2011).

A striking feature is the notable, sudden decrease in the amplitude of the features observed in the transitional subrange, at ~*34.7* km along the profile (red dashed line in Fig. 7). Interestingly, a change in the k_ρ value is also observed at this point. Left of it (*31.5-34.7 km* along profile), the average k_ρ value is $10^{-2.5}$ m^2s^{-1}, while right of this point (*34.7-37 km*), it is $10^{-3.0}$ m^2s^{-1}. Although both values are higher than the average global value for meridional overturning circulation, the highest local average values are obtained in the region where the clearest, largest amplitude features possibly representing KH billows (Sallares et al., 2016), are imaged. Conversely, there is no clear visual correlation between internal wave attributes and k_ρ variations.

H2 is located at ~*95 m* depth and has a length of ~*4.0 km* (*18-22 km* along profile). It was selected because its location coincides with a relatively weak mixing area, according to the k_ρ map (Fig. 5). The corresponding k_x spectrum is shown in Fig. 6b. As in the previous case, we have first calculated k_ρ using the spectral energy values within *1 km*-wide window, moving laterally *30 m* at each step, along the whole reflector length. The average value for the whole horizon is $k_\rho \approx 10^{-4.1}$ m^2s^{-1}, so considerably lower than in H1 but close to the global average value. We have subsequently filtered H2 at the IW (*3000-100 m*) and transitional (*100-30 m*) sub-ranges and compared it with the obtained k_ρ values (Fig. 8). In this case, we have identified three different segments as a function of their average k_ρ value. The first and third segments (*18-19.6 km* and *20.4-22 km*, respectively) display average k_ρ values that coincide, within error bounds, with those of the global ocean average. In particular, we obtain $k_\rho \approx 10^{-4.0}$ m^2s^{-1}, for the first segment, and $k_\rho \approx 10^{-3.8}$ m^2s^{-1}, for the third one. The second or breaking segment, instead, displays a value of $k_\rho \approx 10^{-4.8}$ m^2s^{-1}, which is well below the global ocean average.

H3 is located at ~*80 m* depth and has a length of ~*12 km* (*3.5-15.5 km* along profile). It was selected because its location pass through low and high mixing areas, according to the k_ρ map (Fig. 5). The k_ρ values along the profile have been calculated following the same approach as for the other two reflectors. Its corresponding k_x spectrum is displayed in Fig. 6c. As in the case of H1, we can identify a clear visual correspondence of high mixing values and the largest-amplitude features imaged in the transitional subrange, but not with IWs. Between 9 *km* and 15.5 *km* along the profile the average k_ρ value is $10^{-2.7}\ m^2s^{-1}$, while at the left of it (4-9 *km* along profile) it is $10^{-4.8}\ m^2s^{-1}$. The situation is therefore very similar to the case of H1, and the same correspondence is also observed for the other reflectors along the profile, especially for those located in high mixing areas.

4. DISCUSSION

The spatial variability observed along isopycnals based on the spectral analysis of the seismic data allows identifying a number of local features at different evolutionary stages. These features are the manifestation of relevant oceanographic processes, such as IWs at the internal wave sub-range, hydrodynamic instabilities at the transitional sub-range, and turbulence at smaller scales. Those can be identified by the disruption of the finestructure in the seismic image and the high variability or disappearance of some seismic reflectors.

The large variations observed in the k_ρ vertical profile (Fig. 2), together with the slight tendency to double-diffusion identified in the Turner angle, suggest that the system is prone to be affected by advection processes (e.g. Kunze and Sanford, 1996). Mixing appears to concentrate within the MAW, where the shear values are the highest in the study area, and not deeper than > *110 m*, where there is no remarkable shear and the system is weakly stratified. The shear to strain ratio calculated applying the Gregg89 model ($S_{10}^4/S_{GM}^4 = 21$), indicates that the energy in the IW field is higher than that of the GM model, which usually has a value of 3. We can therefore make the assumption that the energy is distributed in the whole inertial range where the water structures are stable (e.g. Munk, 1981). Similar results were obtained by Holbrook et al. (2013), who registered a shear to strain ratio of *17*. The IWs can therefore be considered as an energy distributor from anisotropic to isotropic motions. The k_ρ value obtained from XCTD and ADCP using Gregg89 model is $k_\rho \approx 10^{-3.0}\ m^2s^{-1}$, whereas we obtain $k_\rho \approx 10^{-2.7} m^2s^{-1}$ using MCS data and the Batchelor59 model. The range of variation in the two cases are also comparable, being the maximum values of $10^{-2.2} m^2s^{-1}$ and $10^{-1.5} m^2s^{-1}$, and the minimum values of $10^{-5.4} m^2s^{-1}$ and $10^{-5.7} m^2s^{-1}$, respectively, for the two methods. These similar values obtained based on different models and using independent techniques are well above the global average, suggesting that the energy transfer to small scales is highly efficient in the studied area.

We find no direct correlation between the presence of IWs and k_ρ. Thus, we interpret that IW-induced mixing is not efficient enough to keep the overturning in the target area (Figs. 7 and 8). No clear correspondence between IW amplitude and k_ρ variation is found along any of the three reflectors. This lack of correlation agrees with Klymak and Moum (2007 a) assumption, suggesting a weak dependence of mixing rates on IW energy. The mixing rates are more reliably measured at smaller scale regimes, in this case the instability-dominated regime that encloses thetransition towards turbulence. In our case, a number of “mixing patches” have been identified at specific

locations in the k_ρ map (Fig. 3), which appear to spatially coincide with areas where shear instability features are located (see reflectors H1 and H3 in figs. 7, 9). These mixing hotspots likely represent a significant source of regional diapycnal mixing at the boundary layer between the MAW and the MW (*30 – 200 m*), which is subject to vertical stratification and shear values of $3.2x10^{-3}\ s^{-1}$. The mixing and energy transfer between these two water masses constitutes the main energy source of the region. The smooth and relatively deep seafloor along the profile (*> 800 m* in average; fig. 10b), likely suggests a small contribution to the generation of mixing hotspots. Given that the MAW-MW boundary layer is subject to shear (Fig. 10a), and taking into account the visual correspondence between the location of the largest amplitude features in the instability-dominated domain and high mixing values, we hypothesize that the direct cause of mixing hotspots is the development of IW shear instabilities. This could explain both the peak values of k_ρ and the high variability along the profile.

The k_ρ values along H1 are over the global average for overturning along most of the reflector ($<k_\rho> \approx 10^{-2.5}\ m^2s^{-1}$), with lower values only at specific points (Fig. 7a). These points are located to the right of 34.7 km, where k_ρ sharply decreases. A similar situation is also observed along H3, reaching a global average ($<k_\rho> \approx 10^{-3.1}\ m^2s^{-1}$).The spatial correspondence between high diffusivity values and the presence of large-amplitude features interpreted to correspond to KH-like shear instabilities by Sallares et al. (2016) at the transitional subrange, is consistent with the hypothesis that a causal relationship exists between the two. This is conceptually equivalent to the mechanism proposed by Gregg (1987), where mixing at the transitional subrange occurs principally at vortex sheets through wave-instability. We could therefore hypothesize that the presence of a vortex sheet left of 34.7 km along profile produces the high mixing values; whereas to the right, there is no vortex sheet and the ocean is more stable. Similar results suggesting a patchy ocean interior, although at larger scales and deeper levels, were also presented by Sheen at al. (2009) and Fortin et al. (2016). Our work confirms these previous results and suggests that the variation is probably due to the high mixing induced by the shear instabilities; which enhances in turn energy transfer to small scales.

5. CONCLUSIONS

We have used acoustic images obtained with a high-resolution MCS system to produce a 2D diapycnal mixing map at the thermocline depth. Our results confirm a high level of diapycnal variability and the presence of marked mixing patches in the water column. The $k_\rho(x, z)$ map obtained by applying the Batchelor59 model to the seismic data, has a strong variability with values ranging between $<k_\rho> \approx 10^{-1.5}\ m^2s^{-1}$, in the high mixing patches (hotspots) and $<k_\rho> \approx 10^{-3.3}\ m^2s^{-1}$, for the background values. The obtained values are high enough to account for overturning at thermocline depths. The mixing hotspots have a characteristic size of *10-15 m* in the vertical dimension, and *1-2 km* in the horizontal one. They are located at different depths within the thermohaline layer, although they appear to concentrate in highly sheared regions. The comparable values obtained with the two independent methods and approaches confirm that HR-MCS is a useful technique to study processes and structures occurring at the sub-mesoscale, which are difficult to be studied otherwise.

The relationship between mixing variability and ocean dynamics at different spatial scales is investigated by analyzing the spectral amplitudes along two seismic horizons in the internal waves and transitional, or instability-dominated, subranges. On one hand, we found no clear correspondence between the location of the mixing patches and the location and amplitude of IWs. Conversely, a visual correspondence exists between the location of shear instabilities and mixing hotspots in different reflectors, suggesting a causal relationship between both features. Areas displaying the most vigorous instabilities coincide with the highest estimated diapycnal mixing values, which are well above the average global value for meridional overturning. This observation suggests that the energy transfer from anisotropic to isotropic scales is highly efficient at thermocline depths within the studied area.

Overall, our study shows that the HR-MCS technique can be used to study sub-mesoscale structures and processes at the thermocline level, provided that the stratification is strong enough to produce acoustic reflectivity that can be recorded by the system. The high-resolution 2D maps produced from the seismic reflectivity could help improving the estimates of the parameters to be incorporated in numerical models of ocean dynamics.

ACKNOWLEDGEMENTS

This work has been fulfilled in the framework of the projects POSEIDON (Ref: CTM2010-25169) and APOGEO (Ref: CTM2011-16001-E/MAR), both funded by the Spanish Ministry of Economy and competitiveness (MINECO). The seismic and oceanographic data were acquired in the framework of the IMPULS survey (Ref: 2003-05996-MAR) also from MINECO, and SAGAS survey (Ref: CTM2005-08071-C03-02/MAR-SAGAS). Helpful comments were provided by Josep Lluis Pelegrí, the Barcelona Center for Subsurface Images (B-CSI), and Diana Francis and David M. Holland from the Center for Global Sea Level Change (CSLC) – NYUAD, Abu Dhabi UAE.

APPENDIX A

Table A1. Parameters used in text

Variable	Value	Description
f	0.00008613 s^{-1}	Coriolis f. at 36°
N	5 cph = 0.00138 s^{-1}	Buoyancy frequency (ocean average)
V	0.207 m s^{-1}	RMS amplitude of velocity fluctuations
υ	0.000001064 m^2 s^{-1}	Kinematic Viscosity
$\mathbf{C_T}$	0.4	Proportionality constant
Γ	0.2	Empirical value of mixing efficiency (Osborn and Cox, 1972).

APENDIX B

Buoyancy Reynolds number

Gargett et al, (1988) use an index to know if the system is isotropic or not, and hence if the allowing know if the buoyancy flux is substantial to generate turbulence and therefore a high mixing level (Thorpe, 2005). The index depends on kinematic viscosity and is called Buoyancy Reynolds number:

$$R_B = \varepsilon / \nu N^2 \quad \text{(B1)}$$

The mean kinematic viscosity in the ocean is $\nu = 1 \times 10^{-6}\ m^2\ s^{-1}$. Some properties of the inertial subrange are consistent with isotropy for values of $R_B < O(10^2)$. To consider anisotropy and avoid serious underestimates of mixing, Smyth and Moum (2000) propose that values > 200 are related with confidence to high mixing levels due to free viscous effects. For our submesoscale regime $R_B = 3200$, a value that reasserts the coherence of the mixing levels calculated. The MCS data present a high confidence level.

References

Biescas B., B. R. Ruddick, M. R. Nedimovic, V. Sallarès, G Bornstein, and J. F. Mojica, Recovery of temperature, salinity, and potential density from ocean reflectivity, J. Geophys. Res. Oceans, 119, 3171-3184, doi:10.1002/2013JC009662, 2014.

Batchelor G. K., Small-scale variation of convected quantities like temperature in turbulent fluid, Fluid Mech., 5, 113-133, 1959.

Chioua J., Bruno M., Vazquez A., Reyes M., Gomiz J., Mañanes R., Alvarez O., Gonzalez C., Lopez L., Gomez-Enri J., Internal waves in the strait of Gibraltar and their role in the vertical mixing processes within the bay of Algeciras, Estuarine, Costal and Shelf Science, Elsevier, 126, 70-86, 2013.

D`Asaro Eric A., Lien Ren-Chien, The Wave-turbulence transition for stratified flows, Journal of physical Oceanography, 1669-1678, July, 2000.

Ferrari Raffaelle and Wunsch Carl, Ocean circulation kinetic energy: Reservoirs, sources, and sinks, Annu. Rev. Fluid Mech, 41: 253-282, 2009.

Fortin et. al., Mapping turbulent diffusivity associated with oceanic internal lee waves offshore Costa Rica. Ocean Sci., 12, 601-612, 2016.

Gargett A and Holloway G, Dissipation and diffusion by internal wave breaking, J. Mar. Res., 42, 15-27, 1984.

Gargett A., The scaling of turbulence in the presence of stable stratification, J. of Geophys. Res., 93, 5021-5036, 1988.

Garrett Christopher and Munk Walter, Internal waves in the ocean, Ann. Rev. Fluid Mech., 11, 339-369, 1979.

Gibson Carl., Keeler R., Bondur Valery, Leung Pak, Prandke H., Vithanage D., Submerged turbulence detection with optical satellites, Coastal Ocean Remote Sensing Conf., Paper 6680-33, San Diego, CA, 2007.

Gregg M. C., Diapycnal mixing in the thermocline: A review, Journal of geophysical research, Vol. 92, Number C5, 5249-5286, 1987.

Gregg M. C., Scaling turbulent dissipation in the thermocline, Journal of geophysical research, Vol. 94, Number C7, 9686-9698, 1989.

Haibin Song, Luis M. Pinheiro, Barry Ruddick and Xinghui Huang. Seismic Oceanography: A new geophysical tool to investigate the thermohalinestructure of the oceans, Oceanography, Prof. Marco Marcelli (Ed.), ISBN: 978-953-51-0301-1, InTech, 2012.

Henyey Frank S. and Wright Jon, Energy and action flow through the internal wave field: an Eikonal Approach, Journal of Geophysical Research, Vol. 91, No: C7, Pages 8487-8495, July 15, 1986.

Holbrook, W., Fer, I., Ocean internal wave spectra inferred from seismic reflection transects. Geophysical Research Letters, Vol. 32, L15604, doi:10.1029/2005GL023733. 2005.

Holbrook, W., Fer, I., Schmitt, R., Lizarralde, D., Klymak. J., Helfrich, C. and Kubichek, R., Estimating oceanic turbulence dissipation from seismic images, Journal of Atmospheric and Oceanic Technology, 2013.Ann. Rev. Fluid Mech., 40, 169-184, 2008.

Holbrook Steven, Fer Ilker, Schmitt Raymond, Lizarralde Daniel, Klymak Jody, Helfrich Cody, and Kubichek Robert, Estimating oceanic turbulence dissipation from seismic images, J. of Atmospheric and Oceanic Tech., Vol. 30, 1767-1788, doi:10.1175/JTECH-D-12-00140.1, 2013.

Klymak M. Jody, Moum N. James, Oceanic isopycnal slope spectra. Part a: Internal waves, Journal of Physical Oceanography. American Meteorological Society, Vol. 37, 1215-1231, 2007.

Klymak M. Jody, Moum N. James, Oceanic isopycnal slope spectra. Part b: Turbulence, Journal of Physical Oceanography. American Meteorological Society, Vol. 37, 1232-1244, 2007.

Kolmogorov, A., Dissipation of energy in the locally isotropic turbulence (English translation 1991). Proc. Roy. Soc. London, A434, 15–17. 1941.

Kunze, E., and Thomas B. Sandford. Abyssal Mixing: Where it is not. J. Phys. Oceanogr. 26, 2286-2296, 1996.

Laurent and Garrett, The role of internal tides in mixing the deep ocean. J. Phys. Oceanogr. 32, 2882-2899, 2002

Li Hua, Yamazaki Hidekatsu, Observations of Kelvin-Helmholz billow in the ocean, Journal of Oceanography, Vol. 57, 709-721, 2001.

Munk W. H., A survey of internal waves and small-scale processes, Evolution of Physical Oceanography, edited by B. A. Warren and C. Wunsch, pp. 264-291, MIT Press, Cambridge, Mass, 1981.

Munk W. Wunsch C., Abyssal recipes II: energetics of tidal and wind mixing, Deep-Sea Research I, Vol. 45, 1977-2010, 1998.

Müller, P. and R. Pujalet : Internal gravity waves and small scale turbulence, proceeding, ‘Aha Huliko’a Hawaiian winter workshop, Hawaiian institute of geophysics, Special Publications, 299 pp., 1984.

Osborn T., & C. S. Cox, Oceanic fine structure, Geophys. Fluid Dyn., Vol. 3, 321-345, 1972.

Osborn T. R, Estimates of the local rate of vertical diffusion from dissipation measurements, Journal of Physical Oceanography, Vol. 10, 83-89, 1980.

Riley J. James, Stratified turbulence: A possible interpretation of some geophysical turbulence measurements, Journal of the Atmospheric Sciences. Vol. 65, 2416-2424, 2008.

Sallarès, V., J. F. Mojica, B. Biescas, D. Klaeschen, and E. Gracia, Characterization of the submesoscale energy cascade in the Alboran Sea thermocline from spectral analysis of high-resolution MCS data, Geophys. Res. Lett., 43, 6461-6468, doi:10.1002/2016GL069782.

Samodurov, A., S., Lubitsky, A., A., and Panteleev, N., A., Contribution of breaking internal waves to structure formation, energy dissipation, and vertical diffusion in the ocean. Phys. Oceanogr., Vol. 6, 3, pp 177 - -190, 1995.

Send Uwe, Font Jordi, Krahmann Gerd, Millot Claude, Rhein Monica, Tintore Joaquin, Recent advances in observing the physical oceanography of the western Mediterranean Sea. Elsevier Science. Progress in Oceanography. Vol. 44, 37-64, 1999.

Sheen L. K., White J. N., Hobbs R. W., Estimating mixing rates seismic images of oceanic structure, Geophysical Research Letters, Vol. 36, L00D04, 2009.

Sheriff Robert and Geldart Lloyd, Exploration Seismology, Cambridge University Press, Second edition, 1995.

Smyth W. D., Moum J. N., Nash J. D., Narrowband oscillations in the upper equatorial ocean. Part II:Properties of shear instabilities, Journal of Physical Oceanography. American Meteorological Society, Vol. 41, 412-428, 2011.

Sreenivasan Katepalli, The passive scalar spectrum and the Obukhov-Corrsin constant, Phys. Fluids, 8, 189-196, 1996.

Smyth William D., Moum James N., Anisotropy of turbulence in stably stratified mixing layers, Physics of Fluids, 12, No. 6, 2000.

Smyth William D., Moum James N., Ocean mixing by Kelvin-Helmholtz Instability, Oceanography, Vol. 25, No. 2, June 2012.

Stewart Robert, Introduction to Physical Oceanography, Department of Oceanography, Texas A&M University, 2008.

Taylor G. I., The spectrum of turbulence, Proc. R. Soc. Lond. A., Vol. 164, No. 919, 476-490, 1937.

Thorpe S. A., Experiments on the instability of stratified shear flows: miscible fluids, J. Fluid Mech., Vol. 46, 299-319, 1971.

Thorpe S. A., The turbulent ocean, Cambridge University Press, Cambridge, 2005.

Waite, Michael L., Stratified turbulence at the buoyancy scale, Physics of fluids, American Institute of Physics, 23, 066602-1, June 2011.

Wesson J.C. and Gregg M.C., Mixing at camarinal sill in the strait of Gibraltar, Journal of Geophysical Research, Vol. 99, No. C5, pages 9847-9878, May 15, 1994.

Woods, J., D.,: Wave induced shear instability in the summer thermocline, J. Fluid Mech., 32, 791-800., 1968.

Wunsch Carl and Ferrari Raffaele, Vertical Mixing, energy, and the general circulation of the oceans, Annual Review Fluid Mech. 36, p. 281-314, 2004.

Yilmaz, O., and S. M. Doherty, Seismic Data Processing, Soc. Of Explor. Geophys, Tulsa, Okla 1987

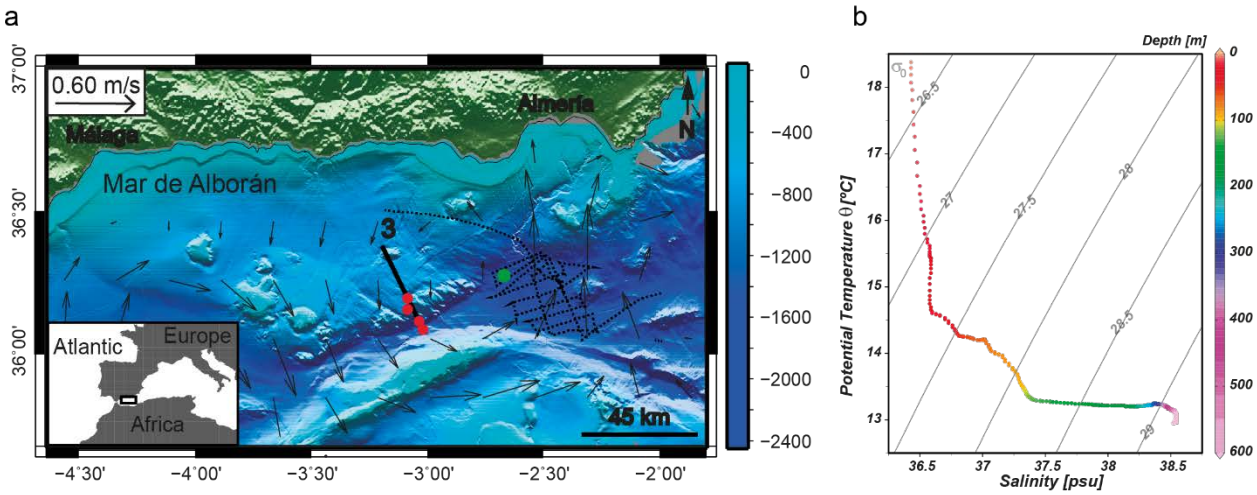

Figure 1. (a) Bathymetric map of the Alboran Sea and location of the data used in the study. HR-MCS profile acquired during the IMPULS-2006 experiment (black line labelled 3), eXpendable Bathy-Thermograph (XBTs) profilers (red circles), eXpendable Conductivity Temperature Depth (XCTD) probe (green circle). Acoustic Doppler Current Profiler (ADCP) lines (black dotted line). Geostrophic velocity for May 17^{t}, 2006 (gray arrows). (b) Temperature-Salinity diagram from XCTD probe. σ_0 is the potential density in kg/m^3. Color scale indicates depth.

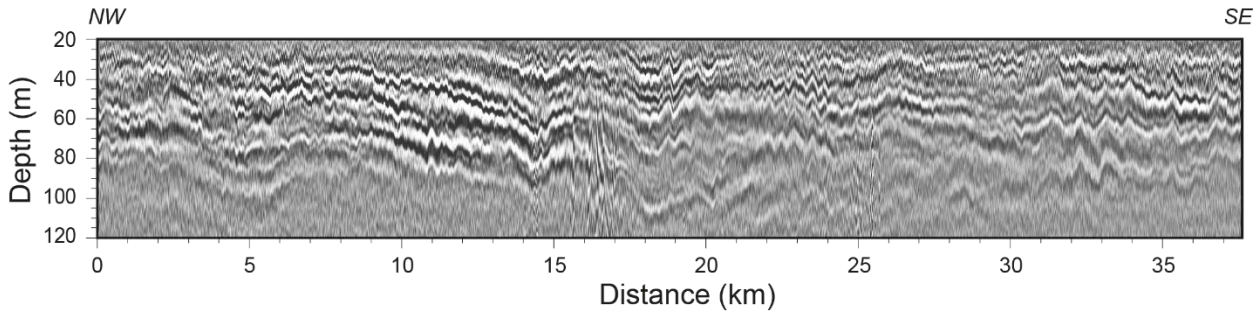

Figure 2. Depth-converted high-resolution multichannel seismic profile (See Fig. 1a for location).

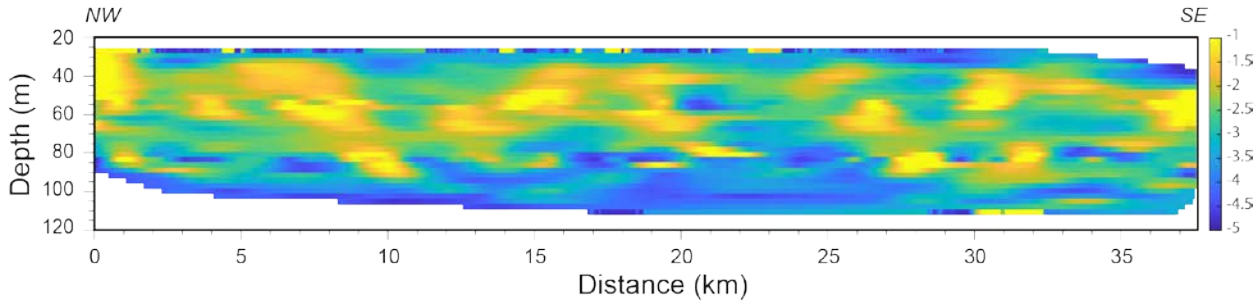

Figure 3. $k_\rho(x, z)$ map obtained along the seismic profile indicated in Fig.1, following the procedure explained in the text.

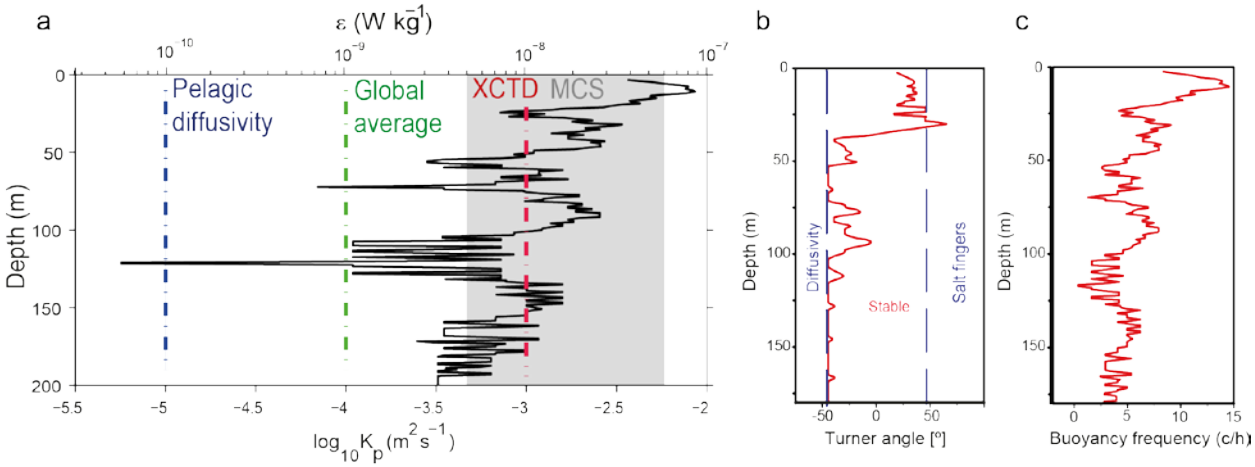

Figure 4. (a) Depth profile of $\varepsilon(z)$ and $k_\rho(z)$ obtained from XCTD and ADCP data and applying Gregg89 model. The blue dotted line is the pelagic diffusivity in the ocean ($k_\rho \approx 10^{-5}\ m^2s^{-1}$), the green dotted line is the global average for overturning ($k_\rho \approx 10^{-4}\ m^2s^{-1}$), the red dotted line is the average vertical profile from XCTD and ADCP data ($k_\rho \approx 10^{-3.0}\ m^2s^{-1}$) and the gray area is the incidence range from MCS data ($k_\rho \approx 10^{-2.7}\ m^2s^{-1}$). (b) Turner angle showing ranges, the blue dotted lines shows where the water column is unstable to diffusivity ($Tu<-45°$), stability ($-45° < Tu <45°$) and prone to salt fingering ($Tu > 45°$), and (c) buoyancy profile calculated with the XCTD data.

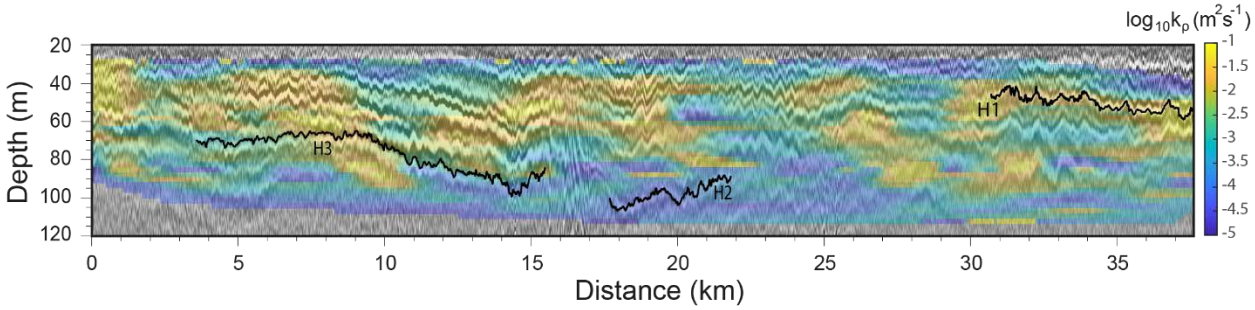

Figure 5. High-resolution $k_\rho(x, z)$ map overlapped with the HR-MCS image. Solid lines labelled H1, H2 and H3, display acoustic reflectors located within relatively high- and low-dissipation areas from Batchelor model.

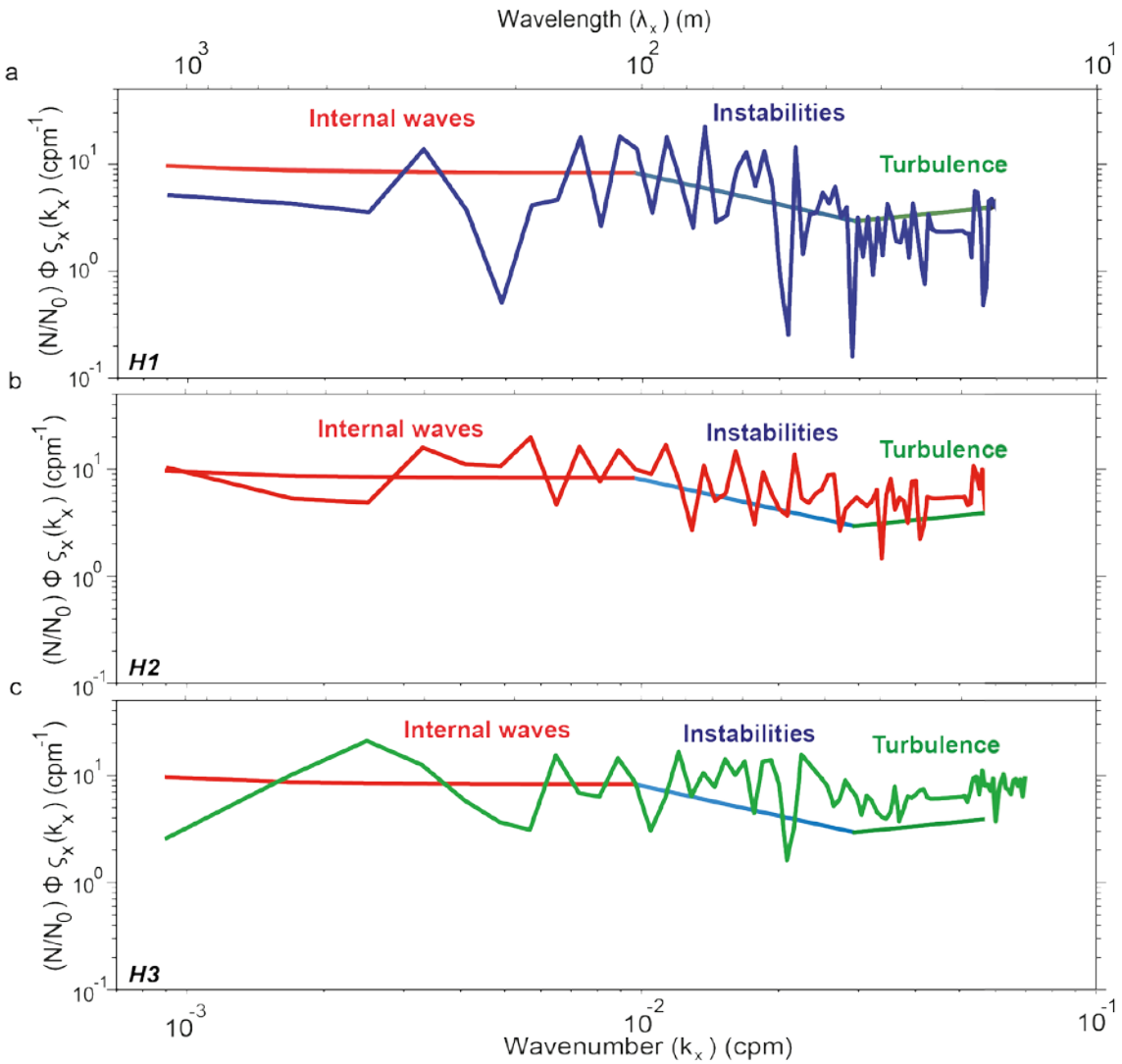

Figure 6. (a) Horizontal spectrum of the vertical displacement of reflector H1 (thick blue line) (see location in Fig. 5). Reference line that follows theoretical slopes of Garret-Munk internal wave
605 model (Garret and Munk, 1979) (red line), Kelvin-Helmholtz instabilities (Waite, 2011) (blue line), and Batchelor model for turbulence (Batchelor, 1959) (green line). The methodology applied to calculate the spectra is described in Sallares et al (2016), (b) and (c) same as in (a) for reflector H2 (red) and H3 (green) in this case.

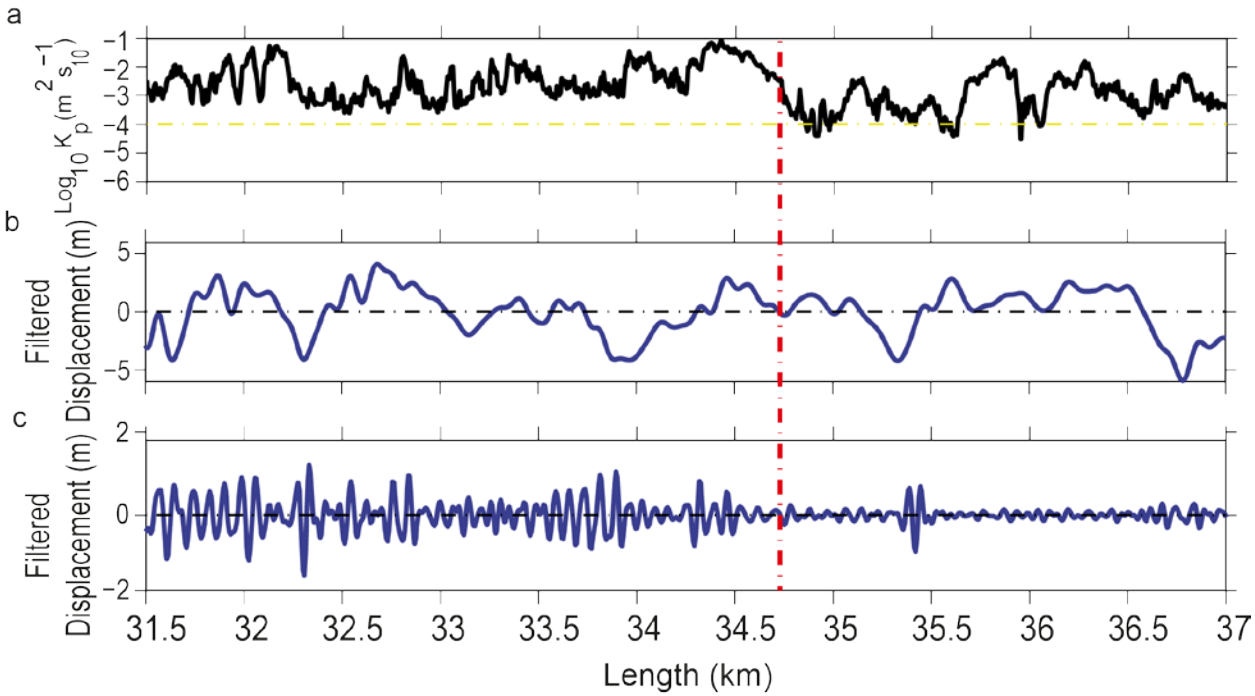

Figure 7. (a) Diapycnal mixing obtained along H1 (see details of calculation in the text). (b) Signal filtered at wavelength ranges of the IW sub-range (*3000-100 m*), (c) and the transitional subrange (*100-33 m*). The dashed red line identifies the "breaking point" referred to in the text.

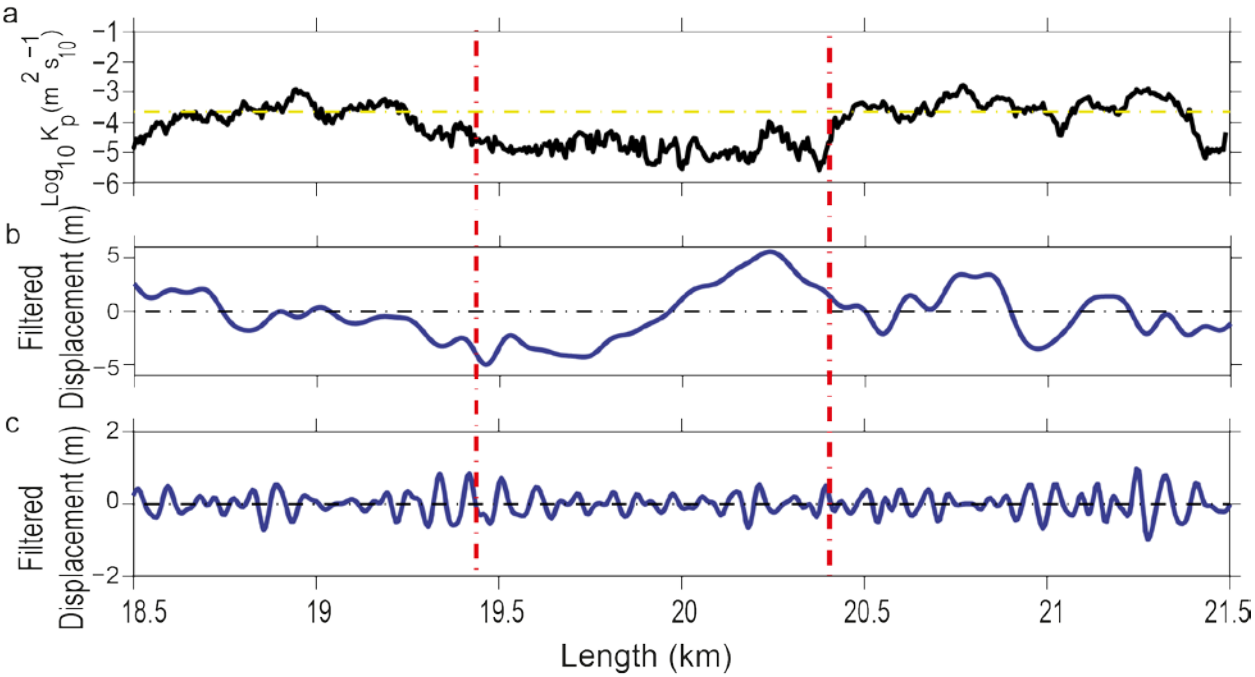

Figure 8. (a) Diapycnal mixing obtained along H2 (see details of calculation in the text). (b) Signal filtered at wavelength ranges of the IW sub-range (*3000-100 m*), (c) and the transitional subrange (*100-33 m*). The dashed red lines identifies the "breaking segment" referred to in the text.

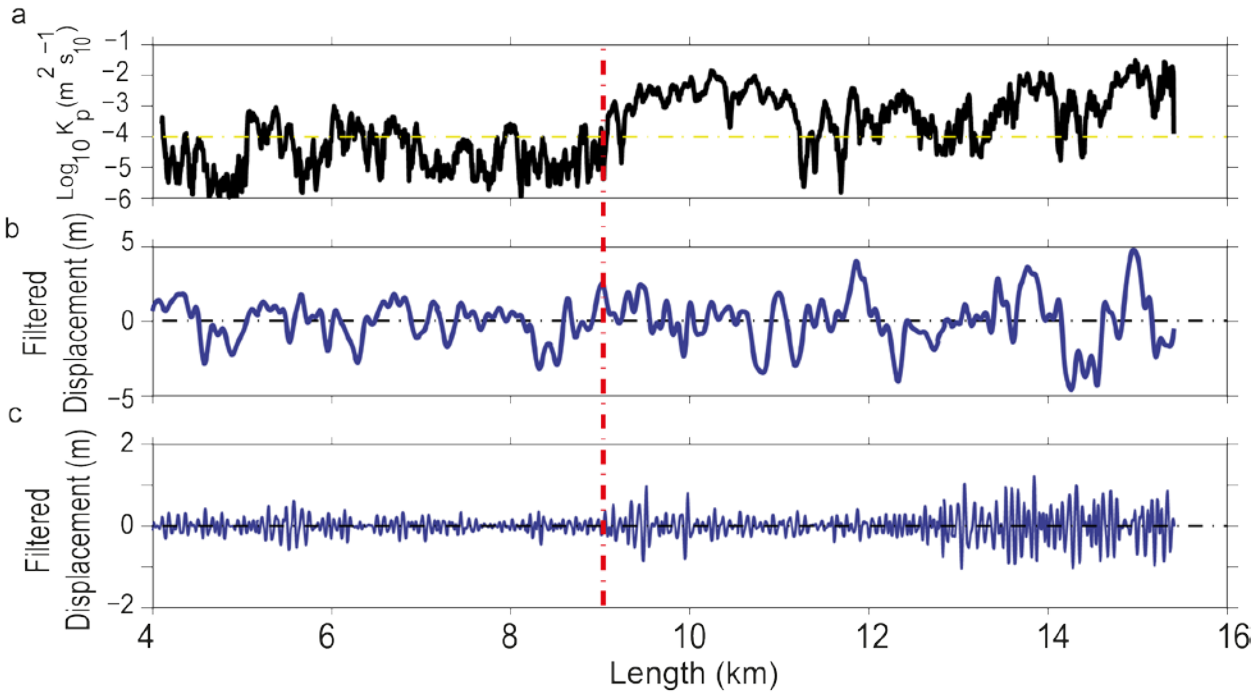

Figure 9. (a) Diapycnal mixing obtained along H3 (see details of calculation in the text). (b) Signal filtered at wavelength ranges of the IW sub-range (*3000-100 m*), (c) and the transitional subrange (*100-30 m*). The dashed red line identify the "breaking segment" referred to in the text.

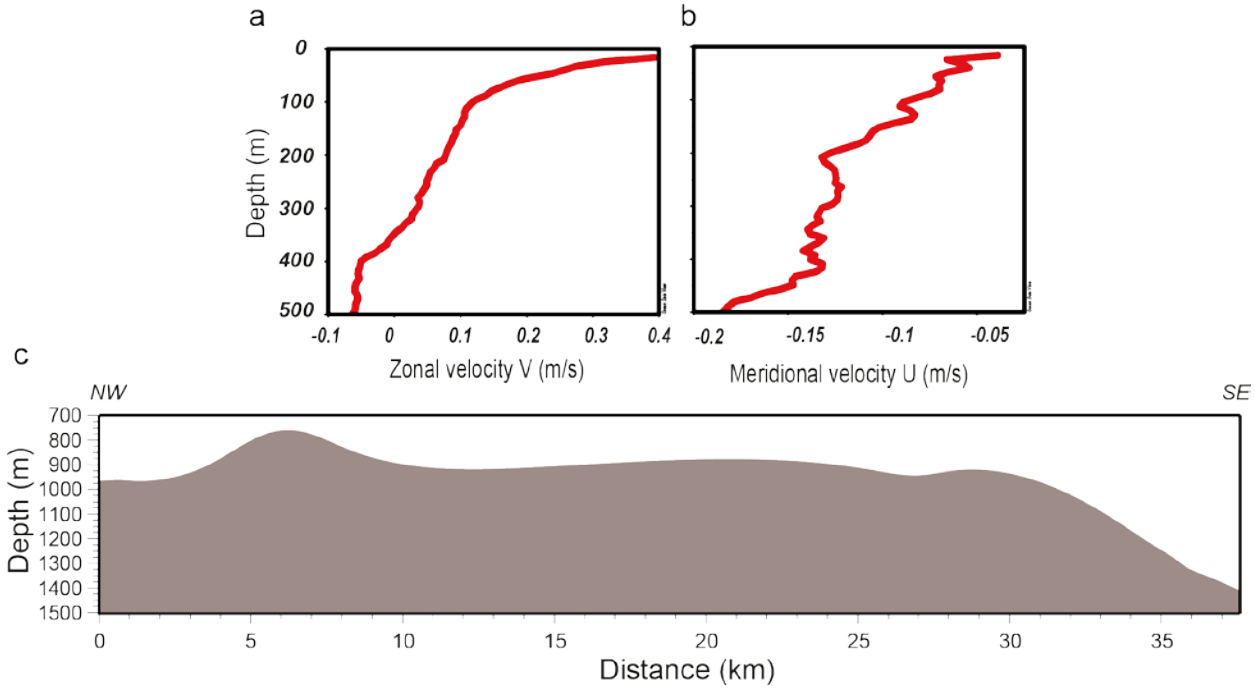

Figure 10. (a) Current velocity profile from ADCP data, SAGAS in May, 2010. (*V*) The zonal velocity variations, and (b) (*U*) the meridional velocity variations according to the depth. (c) Bathymetric profile over the seismic profile.